Characterizing the limitations to the coupling between Saturn's ionosphere and middle magnetosphere

L. C. Ray,[1] M. Galand,[1] L. E. Moore,[2] and B. Fleshman[3,4]

Received 16 March 2012; revised 30 May 2012; accepted 1 June 2012; published 17 July 2012.

[1] Observations of Saturn's ultraviolet and infrared aurora show structures that, when traced along the planetary magnetic field, map to the inner, middle, and outer magnetosphere. From low to high latitudes the structures seen in the UV are the Enceladus footprint, which maps to an equatorial radius of 4 R_S (Saturn radii); a diffuse emission that maps to a broad equatorial region from 4–11 R_S on the nightside; and a bright ring of emission that maps to ~15 R_S. With the exception of the Enceladus spot, the magnetospheric drivers for these auroral emissions are not yet fully understood. We apply a 1D spatial, 2D velocity space Vlasov solver to flux tubes mapping from equatorial radii of 4, 6, 9, and 13 R_S to Saturn's southern atmosphere. The aim is to globally characterize the field-aligned potential structure and plasma density profiles. The ionospheric properties - the field-aligned current densities at the ionospheric boundary, energy intensity profiles and fluxes of the electrons precipitating into the ionosphere - are also determined. We then couple our results to an ionospheric model to calculate the Pedersen conductances at the foot of the relevant flux tubes. We find that for a zero net potential drop between the ionosphere and magnetosphere, there exists a sharp potential drop at ~1.5 R_S along the magnetic field line as measured from the planetary center. The strength of this potential drop is approximately equal to that of the ambipolar potential resulting from the centrifugal confinement of the heavy, cold magnetospheric ion population. We also find that the ionospheric properties respond to changes in the magnetospheric plasma population, which are reflected in the nature of the precipitating electron population. For the flux tube mapping to 9 R_S (−70°), the incident electron energy flux into the ionosphere resulting from a magnetospheric plasma population with a small fraction of hot electrons is an order of magnitude less than that inferred from observations, implying that significant high-latitude field-aligned potentials (up to 1.5 keV) may exist in the saturnian magnetosphere. Calculated ionospheric Pedersen conductances range from 3.0–18.9 mho, and are thus not expected to limit the currents flowing between the ionosphere and magnetosphere.

Citation: Ray, L. C., M. Galand, L. E. Moore, and B. Fleshman (2012), Characterizing the limitations to the coupling between Saturn's ionosphere and middle magnetosphere, *J. Geophys. Res.*, *117*, A07210, doi:10.1029/2012JA017735.

1. Introduction

[2] Saturn is a planet with many types of auroral emissions (see review by *Kurth et al.* [2009]); however, the extent to which these emissions are caused by internally driven magnetospheric processes is unknown. In ultraviolet wavelengths, the brightest of these emissions is the 'main' auroral emission, which exists at ~75° latitude [*Badman et al.*, 2006], varies in strength and position with solar wind conditions [*Clarke et al.*, 2009], and is magnetically conjugate with equatorial radii of ~18–23 R_S (Saturn radii, 1 R_S = 60280 km) [*Bunce et al.*, 2008]. There are two proposed magnetospheric drivers for this emission: the interaction of the saturnian magnetosphere with the solar wind [*Cowley et al.*, 2004, 2008] and the breakdown in corotation of plasma, created from neutral species generated at Enceladus, being transported radially outwards [*Sittler et al.*, 2006]. Equatorward of the main auroral emission, at 'sub-auroral' latitudes, there is a broad diffuse emission centered at 67° with a width of 7° that maps to an equatorial range of ~4–11 R_S [*Grodent et al.*, 2010]. Inferred energy fluxes from this diffuse emission are on the order 0.3 mW/m^2 and are consistent with that expected from pitch angle scattering assuming the magnetospheric parameters presented by

[1]Space and Atmospheres Group, Department of Physics, Imperial College London, London, UK.
[2]Center for Space Physics, Boston University, Boston, Massachusetts, USA.
[3]Homer L. Dodge Department of Physics and Astronomy, University of Oklahoma, Norman, Oklahoma, USA.
[4]Laboratory for Atmospheric and Space Physics, University of Colorado Boulder, Boulder, Colorado, USA.

Corresponding author: L. C. Ray, Space and Atmospheres Group, Department of Physics, Imperial College London, South Kensington Campus, Prince Consort Road, London SW7 2AZ, UK. (l.ray@imperial.co.uk)

0148-0227/12/2012JA017735

Schippers et al. [2008]. Finally, an auroral emission located at the magnetic footprint of Enceladus and driven by the moon's motion through the Saturnian magnetosphere is present at ~64° with an associated brightness in the UV ranging from 1,550 ± 340 to 450 ± 290 Rayleighs (R) [*Pryor et al.*, 2011].

[3] In addition to UV emissions, Saturn has a wealth of auroral H_3^+ infrared (IR) emissions which span from the poles to midlatitudes [e.g., *Stallard et al.*, 2008, 2010; *Badman et al.*, 2011; *Melin et al.*, 2011]. The intensity of the midlatitude auroral signature is 25% of that from the higher-latitude main auroral emission and peaks at ~62°N and ~58°S, which *Stallard et al.* [2010] map to a magnetospheric region of 3–3.95 R_S. *Stallard et al.* [2008, 2010] suggest that this emission may be related to a lag in the plasma angular velocity from corotation near the orbit of Enceladus.

[4] Just as the jovian magnetosphere is populated by plasma from its moon Io, Saturn's rapidly-rotating magnetosphere contains within it a large plasma population that ultimately originates from the moon Enceladus. Although the Saturnian magnetosphere is ultimately dominated by neutrals [*Delamere et al.*, 2007; *Bagenal and Delamere*, 2011], we will focus here on the plasma interaction. Enceladus resides deep inside Saturn's magnetosphere at 3.9 R_S and outgasses ~170–220 kg/s of neutral water based material [*Hansen et al.*, 2011]. This material is subsequently ionized, via photoionization, electron impact ionization, and charge exchange reactions, over a broad equatorial range in the magnetosphere spanning 4–8 R_S [*Sittler et al.*, 2008]. The newly created ions, which previously, as neutral particles, orbited at the local Keplerian velocity, are picked up by the planetary magnetic field and accelerated toward corotation via a current system which runs upwards along the magnetic field lines radially outwards in the equatorial plane, and returns to the planet in a downward current region, finally closing through the ionosphere. In the upward portion of the current system electrons travel along magnetic field lines toward the planet. Outside of 6 R_S, tens of kg/s to 280 kg/s of plasma are transported radially outwards through the Saturnian magnetosphere (see review by *Bagenal and Delamere* [2011, and references therein]), drawing angular momentum from the planet, via the global current system, to stay near corotation. However, the plasma never reaches full corotation. Rather, analysis of Cassini data shows a persistent 20% lag from corotation from 4 R_S to 10 R_S and a monotonic decrease in the plasma angular velocity beyond 10 R_S [*Wilson et al.*, 2008, 2009; *Thomsen et al.*, 2010], indicating that there exists a limitation to the transfer of angular momentum from the planet to the magnetospheric plasma.

[5] At Jupiter, *Hill* [1979] equated the torque exerted upon the radially outward-moving plasma in the magnetosphere with that from the ion-neutral collisions in the planetary atmosphere. This approach allowed the determination of the radial angular velocity profile of the magnetospheric plasma. He found that the transfer of angular momentum was limited by the strength of the planetary magnetic field, radial mass transport rate, and ionospheric Pedersen conductance. As a result, outside a critical equatorial radius the planet would be unable to enforce the rigid corotation of its surrounding magnetospheric plasma. Investigating the 5% corotational lag in the Io torus observed by *Brown* [1983], *Pontius and Hill* [1982] balanced the magnetospheric and ionospheric torques from the local ionization of Iogenic neutrals, determining that the corotational lag could be explained by considering newly charge exchanged ions, which did not change the net plasma density but did change the plasma momentum density, hence increasing the load on the magnetosphere. The relationship of the above systems to Jupiter's main auroral emission and the Io wake emission, respectively, was explored in detail twenty years later [*Hill*, 2001; *Cowley and Bunce*, 2001; *Hill and Vasyliūnas*, 2002; *Delamere et al.*, 2003]. However, the models of the current system driving the main auroral emission did not reconcile the radial mass transport rate of ~500–1600 kg/s with a magnetospheric equatorial mapping location of 20–30 R_J (jovian radii) as determined by observations [*Clarke et al.*, 2004].

[6] Processes which affect the magnetosphere-ionosphere coupling currents have been modeled extensively in the jovian system, including but not restricted to, the subcorotation of the neutral atmosphere, which effectively reduces the ionospheric Pedersen conductance [*Huang and Hill*, 1989], enhancements in electron precipitation which modify the ionospheric Pedersen conductance [*Nichols and Cowley*, 2004; *Ray et al.*, 2010], and field-aligned potentials that develop at high magnetic latitudes [*Nichols and Cowley*, 2005; *Ergun et al.*, 2009; *Ray et al.*, 2010].

[7] Yet few studies investigating the limitations to the magnetosphere-ionosphere coupling currents have been similarly applied at Saturn, despite the wealth of satellite data from Cassini, Voyager 1, and Voyager 2. Rather, models of magnetosphere-ionosphere coupling in the saturnian system use the magnetospheric angular velocity profiles derived from in situ spacecraft measurements along with auroral observations to constrain the ionospheric field-aligned current densities and Pedersen conductances [*Cowley and Bunce*, 2003; *Cowley et al.*, 2008]. *Cowley et al.* [2008] sets an upper bound for the effective ionospheric Pedersen conductance in the southern hemisphere, under summer solstice conditions, of 1–4 mho. These values for the conductance include the effect of the 'slippage' of the neutral atmosphere, relative to the deep planetary rotation. Other approaches specify the magnetospheric plasma angular velocity profile to determine the local mass pickup and radial mass transport rates as a function of the effective ionospheric Pedersen conductance [*Saur et al.*, 2004; *Pontius and Hill*, 2006, 2009]. *Saur et al.* [2004] considers collisions between the magnetospheric ions and neutrals in addition to the radial transport of plasma to describe the magnetospheric angular velocity profile, finding decent agreement with the data for low ionospheric Pedersen conductances of the order ~0.01 mho. Inside of 12 R_S the radial mass transport rates employed in the *Saur et al.* [2004] model are based on the plasma model of *Richardson* [1998]; outside of 12 R_S a transport rate of 40 kg/s was assumed. The analysis of *Pontius and Hill* [2009] requires peak local plasma production rates of ~900 kg/s from charge exchange and radial mass transport rates of 40 kg/s in order to match the observed angular velocity profiles for an assumed ionospheric Pedersen conductance of 0.1 mho.

[8] Independently, using electron density profiles from Cassini Radio Space Science observations, *Moore et al.* [2010] derived values for the ionospheric Pedersen conductances ranging from ~1–8 mho. While these values are consistent with the upper bound predicted by *Cowley et al.*

[2008], they are one to two orders of magnitude larger than those used by *Saur et al.* [2004] and *Pontius and Hill* [2009]. As such, the predicted mass loading rates from the latter two models would need to increase in order to satisfy the observational constraints for the ionospheric conductance. However, as mentioned earlier, the maximum local plasma source rate inferred from models of the Enceladus neutral torus range from ~10s of kg/s to ~300 kg/s.

[9] The aforementioned saturnian models do not consider limitations to the magnetosphere-ionosphere coupling system stemming from the centrifugal confinement of the magnetospheric plasma [*Hill and Michel*, 1976]. The rapid rotation of the saturnian magnetosphere, coupled with an internal plasma source, results in a dense plasma sheet with a scale height of ~2 R_S [*Richardson and Jurac*, 2004]. In addition to the restricted ion mobility owing to the rapid rotation of the magnetospheric plasma, there exists a temperature anisotropy in the heavy magnetospheric water group ions [*Wilson et al.*, 2008] that further limits field-aligned motion. *Su et al.* [2003] and *Ray et al.* [2009] showed that, in the jovian system, the equatorial confinement of the cold, heavy ions results in a field-aligned potential drop at high magnetic latitudes, which ultimately limits the field-aligned current density at the ionosphere and must be considered when relating field-aligned current density to field-aligned potentials, and mapping electric fields between the ionosphere and magnetosphere.

[10] Motivated to reconcile the 20% subcorotation of magnetospheric plasma, ionospheric Pedersen conductances of 1–8 mho, and mass loading rates of 10s of kg/s for radial transport and 100s of kg/s for local charge-exchange processes, we apply a steady state Vlasov code to Saturn's inner and middle magnetosphere to investigate the field-aligned currents running between the ionosphere and magnetosphere. Our goal is to identify any limitations to the currents that transport angular momentum from Saturn to its magnetospheric plasma. Inputs to the model are the ionospheric and magnetospheric plasma populations based on those derived from Cassini data. The outputs are the field-aligned potential structure, ionospheric field-aligned current density, electron intensity profile in energy, and incident electron energy flux, which we then compare to that derived from auroral observations. In order to further explore restrictions to magnetosphere-ionosphere coupling, the derived electron intensity profiles in energy are used to drive an ionospheric model which then calculates the ionospheric Pedersen conductance in the presence of electron precipitation from the magnetospheric plasma population.

[11] Section 2 describes the models used along with our initial assumptions and boundary conditions. Section 3 details the boundary conditions specified at each magnetospheric radius and presents our model outputs. Finally, in section 4 we discuss possible implications of our results and compare with observations before summarizing the key findings in section 5.

2. Model Description

2.1. Vlasov Model

[12] We employ a steady state kinetic Vlasov code [*Ergun et al.*, 2000; *Su et al.*, 2003; *Ray et al.*, 2009] to determine a large-scale, self-consistent solution of the field-aligned potential structure along a magnetic flux tube assuming the following conditions: (i) Zero net potential drop between Saturn's ionosphere and magnetosphere; and (ii) A prescribed plasma composition at each end of the corresponding field line. The field-aligned current density and associated electron energy flux at the top of the ionosphere are also determined.

[13] The Vlasov solver is one-dimensional in space and two-dimensional in velocity space. The spatial domain, which is defined along a magnetic flux tube, is divided into N_S grid points that are evenly spaced along the field line. Similarly the velocity domain is split into $v_{||}$ and $v_{\perp}$, where the $\perp$ and $||$ subscripts denote the components of the velocity perpendicular and parallel to the planetary magnetic field, respectively. For magnetospheric equatorial radial distances (r_{eq}) of 4, 6, 9, and 13 R_S, we focus on the segment of the magnetic flux tube running from the equatorial plane to Saturn's southern hemisphere. The flux tubes with these equatorial locations intersect the planet at latitudes of $-62.1°$, $-67.2°$, $-70.0°$ and $-71.6°$, corresponding to lengths of ~4.6, 7.2, 10.5, and 15.7 R_S, respectively. The large flux tube lengths justify a simple treatment of the altitude of the ionosphere: considering Saturn's oblateness, the ionospheric conducting layer is located at $r = R_S\left(1 - \frac{\cos(90-|\theta|)}{11.1}\right)$ where θ is planetary latitude. We apply the Cassini internal magnetic field [*Dougherty et al.*, 2005] model, which is aligned with the spin axis and includes the 0.037 R_S northward displacement of the dipole, to determine the shape of the magnetic flux tube. To capture the effect of the magnetospheric plasma on the field, we also include the distortion of the magnetic field owing to the ring current [*Bunce et al.*, 2007] for a fixed average value of the sub-solar magnetopause distance of 25 R_S [*Achilleos et al.*, 2008].

[14] The Vlasov solver includes gravitational and centrifugal forces, which dominate at the ionospheric and magnetospheric ends of the flux tube, respectively, and magnetic mirror forces along the flux tube. To calculate the centrifugal forces, we assume that the plasma rotates Saturn at the planetary rotation rate. In actuality, spacecraft measurements show a 20% subcorotating plasma; however using perfect planetary corotation provides an upper limit to restrictions to the field-aligned current density stemming from the centrifugal confinement of the plasma. Figure 1 shows the gravitational (dotted lines) and centrifugal (dashed lines) potentials as a function of distance along the flux tube for water group ions at $r_{eq} = 9$ R_S. The solid line is the sum of the two potentials which has a minimum at ~2 R_S kronographic along the flux tube. The left- and right-hand sides are the ionospheric and magnetospheric boundaries, respectively.

[15] The boundary conditions for the Vlasov code are the plasma populations at the ionosphere and equatorial magnetosphere as well as the net potential drop between the two regions. The ionospheric plasma population, described in Table 1, is prescribed as a fluid and held fixed for all runs. The magnetospheric boundary conditions vary with equatorial distance from Saturn as illustrated in Table 2. Magnetospheric plasma species are assigned as either Kappa or Maxwellian velocity distributions based on Cassini observations. Magnetospheric protons are described as a spatial Boltzmann distributions for ease of computation.

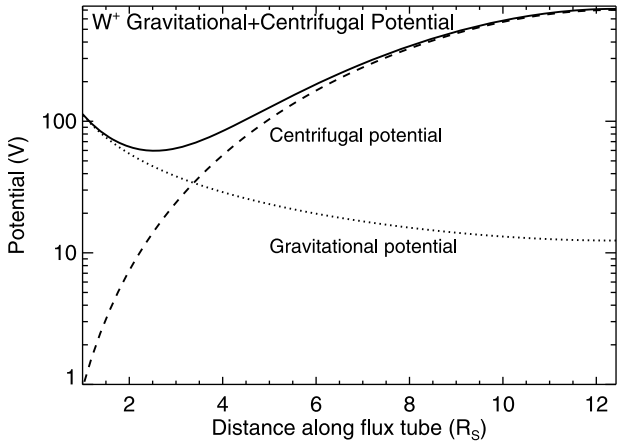

Figure 1. Gravitational and centrifugal potentials for water group ions along the flux tube mapping to 9 R_S in the equatorial plane. The ionospheric end of the flux tube is on the left and the magnetospheric end is on the right.

[16] Kappa and Maxwellian velocity distribution functions are broken into $N_v \times N_v$ velocity space elements ($N_v = 100$), each of which are then propagated along the flux tube. The maximum velocity considered is user selected and affects the runtime of the Vlasov solver. We find that the solutions do not change significantly for maximum velocities above $6v_{th}$, $v_{th} = \sqrt{\left(\frac{2T}{m}\right)}$ where T is the average thermal energy of the distribution and m is the mass of the species. We use this value to initialize our cold electron and heavy ion distribution functions. The maximum velocity of the hot electrons corresponds to an energy of 50 keV. An estimated field-aligned potential structure, $\Phi_0(s)$, initializes the model and then, using conservation of energy and the first adiabatic invariant, $\mu = \frac{mv_\perp}{2B}$, the velocity space distributions of the plasma are calculated at each spatial step along the flux tube. Species defined as Boltzmann distributions are spatially treated with the density varying as $n_{Boltzmann}(s) = n_0 e^{(-\Phi_{Tot}(s)/T_0)}$ where T_0 and n_0 are the temperature and density of the species in the equatorial plane, and $\Phi_{Tot}(s)$ is the field-aligned potential structure given by the sum of the gravitational, centrifugal, and electric potentials.

[17] The model solves Poisson's equation along the field line, calculating the error, $\xi(s)$ at each spatial step

$$\xi(s) = \nabla^2\Phi(s) + \frac{e}{\epsilon_0}[n_i(s) - n_e(s)] \quad (1)$$

where e is the charge of the electron, ϵ_0 is the permittivity of free space, and $n_i(s)$ and $n_e(s)$ are the ion and electron densities along the flux tube as calculated from the distribution functions. We iteratively adjust the electric potential, $\Phi(s)$, to minimize the total error $\int_s \xi(s)$, yielding a steady state solution along the field line. The gravitational and centrifugal potentials are dictated by the planetary mass, rotation rate, and distance from the center of the planet; and spin axis, respectively, and hence fixed for a given flux tube and particle species. Therefore changing the electric potential is equivalent to adjusting the ambipolar field-aligned potential. The spatial size of the grid ($ds \sim 10000$ km) is significantly larger than the Debye length ($\lambda_D < 1$ km); hence the first term on the right-hand side of equation (1) is negligible, essentially resulting in a quasi-neutral solution.

[18] The net potential drop is held at zero, and thus the resulting potential structure along the magnetic field line is that of the ambipolar potential that develops owing to the charge separation caused by the differing degrees of centrifugal confinement of the ions and electrons. The quasi-neutral density structures are then used to calculate the field-aligned current density. Here, we cite the field-aligned current density at the ionospheric boundary. The electron flux profile of the precipitating electrons, in particles s^{-1} cm^{-2} eV^{-1}, is given by $I_e(E) = \pi n_{e_M} e \frac{v^2}{m_e} f(\vec{v})$ where n_{e_M} is the density of magnetospheric electrons at the ionospheric end of the flux tube; $e = 1.6022 \times 10^{-19}$ J/ev is the conversion from Joules to eV; $m_e = 9.11 \times 10^{-31}$ kg is the mass of the electron; $f(\vec{v})$ is the distribution function of the electrons, and $\vec{v}$ is the velocity of the precipitating electrons. The factor of π reflects that we approximate the precipitating particles as isotropic over the upward hemisphere (from a magnetospheric point

Table 1. Composition and Temperature of the Ionospheric Plasma [*Kliore et al.*, 2009] (Left Boundary)

Species	Density (cm^{-3})	Temperature	Type
H^+	2×10^4	0.059 eV	fluid
e^-	2×10^4	0.059 eV	fluid

Table 2. Compositions and Temperatures of the Ion and Electron Species Specified in the Magnetosphere at the Equatorial Plane (Right Boundary in Figures)[a]

Species	Density (cm^{-3})	Temperature (eV)	Type
4 R_S[b]			
W^+	55	30; $T_\perp/T_\parallel = 5$	Maxwellian
H^+	5	4	Boltzmann
e^-	60	5	kappa, $\kappa = 3$
6 R_S[c,d]			
W^+	30.68	74.6; $T_\perp/T_\parallel = 4.83$	Maxwellian
H^+	2.35	8.3	Boltzmann
e_h^-	0.03	1000.0	kappa, $\kappa = 3.6$
e_c^-	33.00	2.0	kappa, $\kappa = 5.5$
9 R_S - 'trended' case[c,d]			
W^+	4.62	165.0; $T_\perp/T_\parallel = 2$	Maxwellian
H^+	0.66	27.0	Boltzmann
e_h^-	0.18	1800.0	kappa, $\kappa = 3.6$
e_c^-	5.10	14.0	kappa, $\kappa = 2.0$
9 R_S - 'lower-bound' case[d,e]			
W^+	4.62	165.0; $T_\perp/T_\parallel = 2$	Maxwellian
H^+	0.66	27.0	Boltzmann
e_h^-	0.02	1000.0	Maxwellian
e_c^-	5.26	6.0	kappa, $\kappa = 3$
13 R_S[c,d,f]			
W^+	0.43	416.0; $T_\perp/T_\parallel = 2$	Maxwellian
H^+	0.24	30.0	Boltzmann
e_h^-	0.13	1177.0	kappa, $\kappa = 3.77$
e_c^-	0.54	19.6	kappa, $\kappa = 1.97$

[a]Water group ions are assumed to have a mass of 17 amu.
[b]Population based on *Fleshman et al.* [2010].
[c]Electron population based on *Schippers* [2009].
[d]Ion population based on *Wilson et al.* [2008].
[e]Electron population based on *Schippers et al.* [2012].
[f]Ion population based on *Thomsen et al.* [2010].

of view electrons precipitate into the ionosphere). The solid angle integration from intensity to flux is $\int_0^{2\pi} \cos\theta d\Omega = 2\pi \int_0^1 \mu d\mu$ where Ω is the solid angle integrated over a single hemisphere to yield 2π, $\mu = \cos\theta$ and θ is the pitch angle. The incident electron energy flux is thus the integral over energy of the intensity times energy.

2.2. Ionospheric Model

[19] Finally, the Pedersen conductances are calculated using the above electron intensity profiles as input to a solar and auroral energy deposition model [*Galand et al.*, 2011] coupled self-consistently to a model of Saturn's ionosphere [*Moore et al.*, 2004, 2008, 2010]. The reader is referred to these publications for detailed descriptions of the model calculations and sensitivities; the conditions specific to this analysis are detailed below. We assume southern summer solstice conditions (solar declination $-26.73°$). The neutral atmosphere at the latitudes of interest, as a function of local time, is extracted from the 3D Saturn Thermosphere Ionosphere Model (STIM) [*Mueller-Wodarg*, 2012] assuming the same solar seasonal conditions as the ionospheric model. In addition to incident energy flux from precipitating electrons, solar radiation corresponding to quiet solar conditions (F10.7 $\sim$ 70) is also considered [*Galand et al.*, 2009]. The fully-coupled model is presented in *Galand et al.* [2011] to which the reader is referred for a detailed description. We scale the effective reaction rate, $k_1^* = k_1 \frac{[H_2(\nu \geq 4)]}{[H_2]}$, for the chemical reaction $H^+ + H_2(\nu \geq 4) \rightarrow H_2^+ + H$, hereafter R1, as appropriate for sub-auroral regions. For sufficiently high vibrational energies, $\nu \geq 4$, reaction R1 becomes exothermic and rapidly occurs. The reaction rate, k_1, is constrained through laboratory plasma experiments [*Huestis*, 2008]; however the relative abundance of $H_2(\nu \geq 4)$ to H_2, $\frac{[H_2(\nu \geq 4)]}{[H_2]}$, in Saturn's atmosphere is less well known. We take the ratio from *Moses and Bass* [2000] as a baseline and scale k_1^* to adjust $\frac{[H_2(\nu \geq 4)]}{[H_2]}$. Reaction R1 transforms the long-lived ion H^+ into H_2^+, which is quickly converted into H_3^+, which in turn has a shorter lifetime than H^+. Consequently, increasing k_1^* yields a decrease in the electron density, and hence a decrease in the Pedersen conductance. *Moore et al.* [2010] found that a scaling of the effective reaction rate to 0.25 k_1^* best fit Cassini radio space science observations and is reasonable for an ionosphere influenced primarily by incident solar FUV flux. When intense auroral electron precipitation is present, the relative abundance of $H_2(\nu \geq 4)$ is expected to be enhanced and as such, the scaled rate of k_1^* is increased to 2 k_1^* [*Galand et al.*, 2011]. However, we note that despite doubling k_1^* there exists a net enhancement of the ionospheric density, owing to the increased ionization from electron precipitation and thus an overall increase in the Pedersen conductance in regions with intense auroral precipitation. In the present analysis we select reaction rate values of 2 k_1^* and 0.6 k_1^* for hard and soft auroral precipitations, respectively.

3. Modeling Results

[20] In order to characterize the ionospheric field-aligned currents, precipitating electron intensities, incident electron energy fluxes, and Pedersen conductances at latitudes mapping to Saturn's inner and middle magnetosphere, we apply the Vlasov code to flux tubes intersecting the equatorial plane at 4, 6, 9, and 13 R_S. We fix the ionospheric boundary for all runs to have a plasma composition of $n_{H^+} = n_{e^-} = 2 \times 10^4$ cm^{-3} and $T_{H^+} = T_{e^-} = 680$ K ~ 0.059 eV [*Kliore et al.*, 2009] as shown in Table 1. The properties of Saturn's magnetospheric plasma vary strongly with radial distance. For this reason, we base the magnetospheric boundary conditions on Cassini CAPS data analyses [*Schippers et al.*, 2008; *Wilson et al.*, 2008; *Thomsen et al.*, 2010; *Schippers et al.*, 2012] and modeling efforts [*Fleshman et al.*, 2010]. In addition to modeling how radial variations in the magnetospheric plasma population affect the ionospheric properties, we also assess how changes in the magnetospheric population for the flux tube mapping to $r_{eq} = 9\ R_S$ affect our results. In the following sections, we describe magnetospheric populations used and present our results for the field-aligned ambipolar potential and density structures, along with the predicted ionospheric parameters.

[21] Magnetospheric protons are treated as Boltzmann species in all cases for ease of computation. The proton density peaks $\sim$1 R_S off the equatorial plane owing to the ambipolar field-aligned potential. Therefore, the proton density is non-monotonic with distance along the flux tube and as such there is a phase space hole at low energies for equatorial latitudes. Unfortunately, this phase space hole prevents error reduction and the determination of a steady state quasi-neutral Vlasov solution. A Boltzmann treatment, while a simplification of the proton distribution's properties that ignores the velocity space distribution, allows us to obtain Vlasov solutions.

[22] *Wilson et al.* [2008] determined that from 6 R_S – 10 R_S Saturn's magnetospheric protons have a temperature anisotropy of $T_\perp / T_\parallel \sim 2$, where $T_\perp$ and $T_\parallel$ are the energies perpendicular and parallel to the magnetic field, respectively. As the simple Boltzmann treatment does not include temperature anisotropies, we use the effective temperature, $T_{eff} = (2T_\perp + T_\parallel)/3$, to describe the magnetospheric protons. For Maxwellian distributions, the temperature anisotropies are included in the Vlasov calculation.

[23] Kappa distributions are defined as [*Baumjohann and Treumann*, 1996, p. 120]

$$f_\kappa(W) = n\left(\frac{m}{2\pi\kappa W_0}\right)^{3/2} \frac{\Gamma(\kappa+1)}{\Gamma(\kappa-1/2)} \cdot \left(1 + \frac{\left(\sqrt{(W)} - \sqrt{(W_S)}\right)^2}{\kappa W_0}\right)^{-(\kappa+1)} \quad (2)$$

where $W_0 = k_B T(1–3/2\kappa)$ is the particle energy at the peak of the distribution, T is the average thermal energy, W_S is the shift energy, and κ provides the shape of the power law tail. In this analysis, we cite the average thermal energy, T, and κ to characterize kappa distributions.

3.1. Solution for Flux Tube Intersecting 4 R_S

[24] The magnetospheric plasma population at 4 R_S is based on the baseline 'best-fit' solution from the modeling analysis of *Fleshman et al.* [2010]. In brief, their analysis applies a physical chemistry model of the Enceladus torus to study how variations in the neutral source rate, hot electron temperature, hot electron density, and radial transport

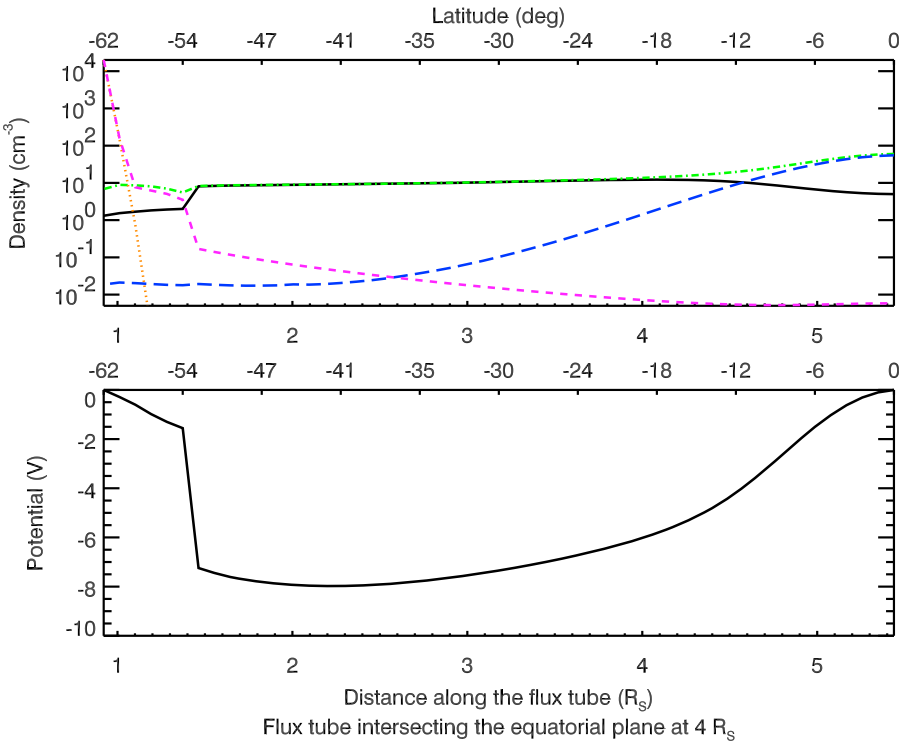

Figure 2. Plasma density and ambipolar potential profile along the magnetic flux tub mapping to 4 R_S. The plasma species are magnetospheric electrons (green, dot-dashed line), water group ions (blue, long dashed line), and protons (black, solid line), and ionospheric protons (pink, dashed line) and electrons (orange, dotted line).

timescales affect the composition and density of this region. Ion and neutral sources and losses include charge exchange, impact ionization, photoionization, radial transport, dissociative recombination, and recombination processes. Their baseline solution is that for which the model output best matches the water group, proton, and electron densities and temperatures inferred from Cassini CAPS data [*Fleshman et al.*, 2010, Table 1].

[25] Here, we assume analytical distributions whose parameters are consistent with the *Fleshman et al.* [2010] baseline solution. The magnetospheric plasma composition is as follows: a kappa distribution of electrons with a density of n_e = 60 cm^{-3}, temperature of T_e = 5 eV, and κ = 3; a Boltzmann proton distribution with a density of n_{H^+} = 5 cm^{-3} and effective temperature of T_{H^+} = 4 eV; and a Maxwellian distribution of water group ions with a density of n_{W^+} = 55 cm^{-3}, effective temperature of T_{W^+} = 30 eV, and temperature anisotropy of $T_\perp/T_\parallel$ = 5. We assume a mass of 17 amu for the water group ions. The electron population is approximated as a kappa distribution rather than two Maxwellians for ease of computation.

[26] The quasi-neutral density and ambipolar potential structure are shown in Figure 2 with the ionospheric and magnetospheric ends of the flux tube on the left- and right-hand sides, respectively. The proton density peaks at ~1 R_S off the equatorial plane, owing to the ambipolar potential and consistent with plasma density models based on Cassini RPWS and CAPS observations [*Sittler et al.*, 2008; *Persoon et al.*, 2009]. The heavier water group ions are confined to the equatorial plane. At the ionospheric end of the flux tube there exists an ambipolar potential of ~1.5 V which restricts the mobility of the ionospheric electrons. The ambipolar potential on the magnetospheric end of the flux tube is larger with a maximum magnitude of ~8 V at ~3.2 R_S above the equatorial plane. Nearly the entire ambipolar potential is dropped within ~0.15 R_S which results in a narrow acceleration region at ~1.6 R_S above the ionosphere (N.B. the x-axis starts at 0.9 R_S owing to Saturn's oblateness). At high latitudes, coincident with the sharp potential drop, the density is dominated by magnetospheric electrons and ionospheric protons. The ionospheric field-aligned current density is 1.514 μA/m^2.

[27] Figure 3a displays the ionospheric electron intensity profile as a function of electron energy where the thick blue line represents the modeled results. The minimum energy of the precipitating electrons is 8 eV as expected in the presence of an 8 V potential drop. As detailed in section 2.1, the maximum energy of the distribution is set to $6v_{th}$ for computational purposes, here equal to 180 eV. However, the higher energy tail of the distribution is present in the physical system and we extrapolate the modeled curve to a maximum energy of 200 keV as shown by the thin line. The mean energy and energy flux of the precipitating electrons into the ionospheric model are 27 eV and 0.00472 mW/m^{-2}, respectively. This yields an ionospheric Pedersen conductance ranging from 3.0–3.8 mho at −62.1° where the range represents local time variability. We use 0.6 $k_\parallel^*$ as appropriate for the soft electron precipitation indicated by the low energy

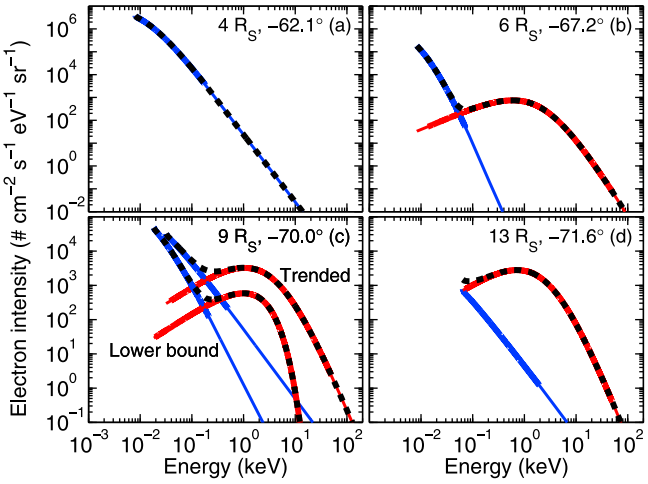

Figure 3. Electron intensity profile at the ionosphere for flux tubes mapping to magnetospheric equatorial distances of (a) 4, (b) 6, (c) 9, and (d) 13 R_S. For the flux tube mapping to 9 R_S, both the 'trended' and 'lower-bound' cases. The cold and hot electron contributions are displayed in blue and red, respectively. The total electron intensity in energy is shown by the black dashed line. These profiles are input for the auroral energy deposition model.

flux. Background conductances from solar energy flux alone ($0.25\ k_1^*$) range from 2–3 mho and thus, at the base of the flux tube mapping to r_{eq} = 4 R_S, the ionospheric conductance is not strongly affected by the electron precipitation.

3.2. Solution for Flux Tube Intersecting 6 R_S

[28] For the flux tube mapping to r_{eq} = 6 R_S, the magnetospheric plasma composition is based on the analysis of Cassini CAPS data. *Schippers* [2009] performed a statistical analysis on a dozen Cassini orbits to find a median electron population consisting of: a kappa distribution of cold electrons with a density of n_{e_c} = 33.0 cm^{-3}, temperature of T_{e_c} = 2 eV, and κ = 5.5; and a kappa distribution of hot electrons with a density of n_{e_h} = 0.03 cm^{-3}, temperature of T_{e_k} = 1000 eV, and κ = 3.6. The ion composition is based on that presented by *Wilson et al.* [2008]; however the densities have been adjusted such that the initial magnetospheric plasma is quasi-neutral, i.e., $n_{H^+} + n_{W^+} = n_{e_c} + n_{e_h}$. The ion population is thus: a Boltzmann distribution of protons with a density of n_{H^+} = 2.35 cm^{-3} and effective temperature of T_{H^+} = 8.3 eV; and a Maxwellian distribution of water group ions with a density of n_{W^+} = 30.68 cm^{-3}, effective temperature of T_{W^+} = 74.6 eV, and temperature anisotropy of $T_\perp/T_\parallel$ = 4.83. We assume a water group mass of m_{W^+} = 17 amu, consistent with the *Wilson et al.* [2008] analysis, and reflecting the presence of O^+, OH^+, H_2O^+ and H_3O^+ ions.

[29] Figure 4 displays the quasi-neutral density and ambipolar potential structures along the magnetic flux tube. Similar to the r_{eq} = 4 R_S case, the proton density peaks ~1.5 R_S above the equatorial plane. The ionospheric ambipolar potential maximizes at ~2 V and the magnetospheric ambipolar potential has a maximum magnitude of 8.1 V at 5.5 R_S above the equatorial plane. A sharp potential drop over a narrow width of 0.1 R_S along the field exists at 1.6 R_S. On the ionospheric end of the sharp potential drop, there exists a

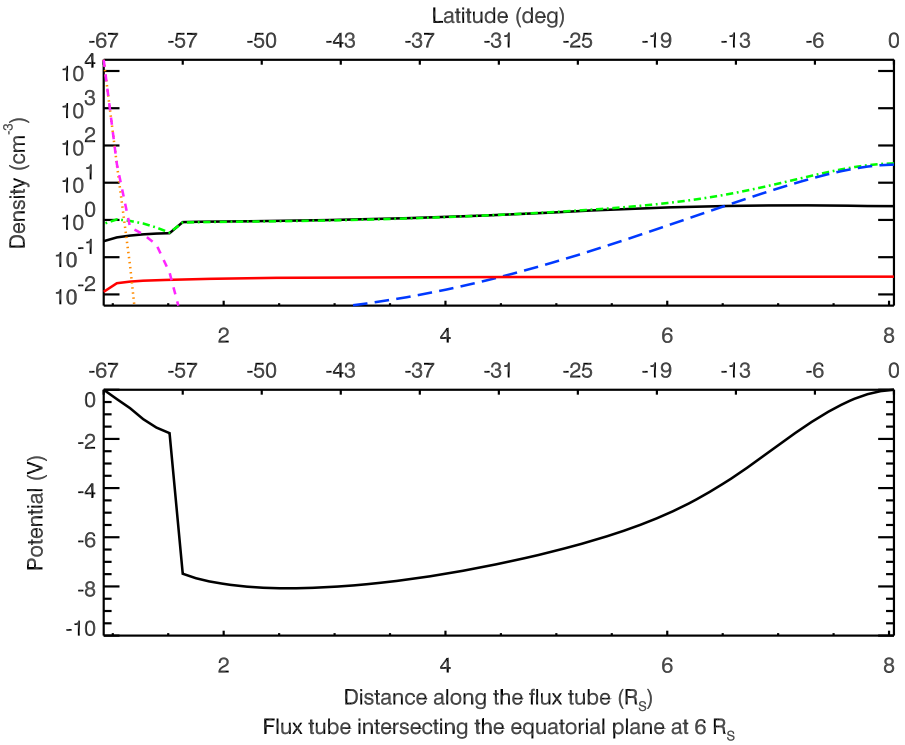

Figure 4. Plasma density and ambipolar potential profile along the magnetic flux tub mapping to 6 R_S. The plasma species are magnetospheric cold electrons (green, dot-dashed line), water group ions (blue, long dashed line), protons (black, solid line) and hot electrons (red, dot-dot-dot-dashed line), and ionospheric protons (pink, dashed line) and electrons (orange, dotted line).

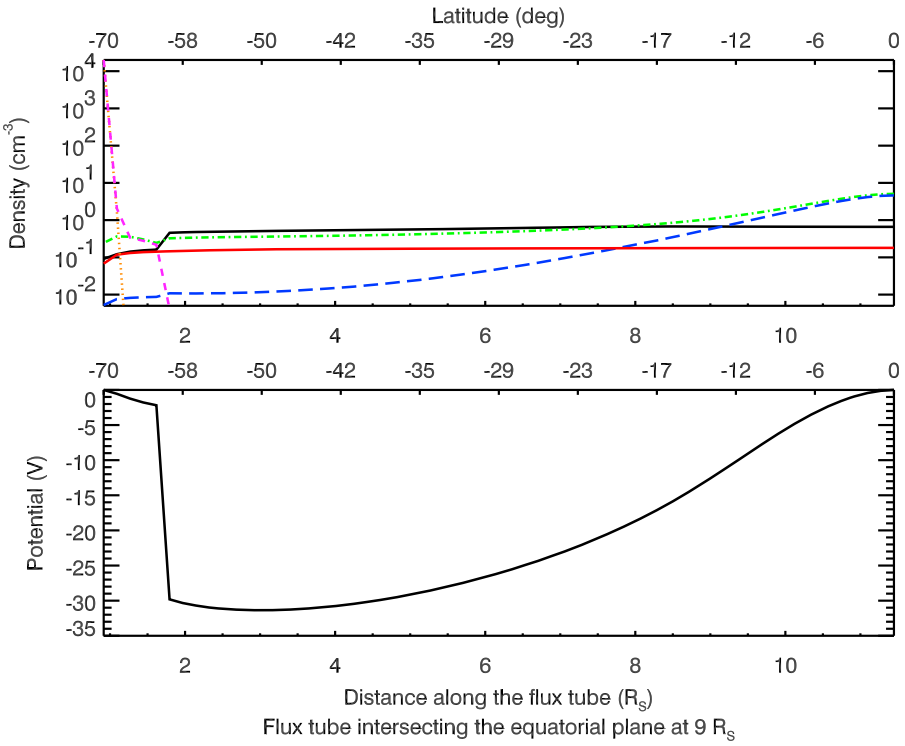

Figure 5. Same as Figure 4 but for the flux tube mapping to 9 R_S. The magnetospheric electron population boundary condition is based on the analysis of *Schippers* [2009].

density cavity spanning 0.5 R_S created by the acceleration of electrons through the potential structure. Owing to their greater density contribution, the field-aligned current is carried predominately by the cold electrons. The net ionospheric field-aligned current density ($j_{\|i}$) is 0.186 μA/m^2, only 0.024 μA/m^2 or ~11% of which is carried by the hot electrons.

[30] The electron intensity profiles are shown in Figure 3b. The cold electrons, in blue, dominate the electron intensity at low energies while the hot electron population, in red, provides the largest contribution above ~70 eV. Most of the energy is delivered to the ionosphere via the hot electron population with cold and hot electron energy fluxes of 5.26×10^{-5} mW/m^2 and 0.0241 mW/m^2, respectively. Extrapolating the energy intensity profiles past the maximum energy of 72 eV from the Vlasov model to a maximum energy of 200 keV, as shown by the thin blue and red lines, yields a net energy flux of approximately 0.0248 mW/m^2. In the presence of such an electron precipitation, the ionospheric Pedersen conductance at −67.2° ranges from 5.06 to 5.85 mho over a Saturnian day, using 0.6 k_1^*.

3.3. Solutions for Flux Tube Intersecting 9 R_S

[31] We present two cases for the flux tube mapping from −70.0° latitude to r_{eq} = 9 R_S in sections 3.3.1 and 3.3.2; one which uses the 'trended' electron densities that are determined following the method described in section 3.2 [*Schippers*, 2009], and a second that accounts for the re-calibration of the Cassini CAPS electron spectrometer [*Lewis et al.*, 2010] that subsequently results in decreased hot electron densities [*Schippers et al.*, 2012]. In order to study the effects of varying electron populations, we hold the ion properties fixed for both cases with a Boltzmann distribution of protons with a density of n_{H^+} = 0.66 cm^{-3} and effective temperature of T_{H^+} = 27.0 eV; and a Maxwellian distribution of water group ions with a mass of m_{W^+} = 17 amu, density of n_{W^+} = 4.62 cm^{-3}, effective temperature of T_{W^+} = 165.0 eV, and temperature anisotropy of $T_\perp/T_\|$ = 2. The ion properties are from the analysis of *Wilson et al.* [2008]; however the ion densities have been adjusted to equal those of the electrons such that the equatorial magnetospheric plasma is quasi-neutral.

3.3.1. Case 1: Large Fraction of Hot Electrons

[32] For the 'trended' case [*Schippers*, 2009], the magnetospheric electron population consists of a kappa distribution of cold electrons with a density of n_{e_c} = 5.1 cm^{-3}, temperature of T_{e_c} = 14.0 eV, and κ = 2; and a kappa distribution of hot electrons with a density of n_{e_h} = 0.18 cm^{-3}, temperature of T_{e_h} = 1800.0 eV, and κ = 3.6.

[33] Figure 5 displays the field-aligned density and ambipolar potential structure for the quasi-neutral solution. The density of the magnetospheric hot electrons is nearly constant along the magnetic flux tube; however, the density of the magnetospheric cold electrons falls off with distance from the equatorial plane. On the ionospheric edge of the sharp field-aligned potential drop, there is a narrow density cavity carved out by the acceleration of particles through the drop. The maximum magnetospheric ambipolar potential is 31.4 V, increasing from the previous cases owing to the higher rotation velocity at larger equatorial distances from the planet, while the ionospheric ambipolar potential remains ~2 V as the surface gravity is independent of the flux tube's equatorial mapping distance.

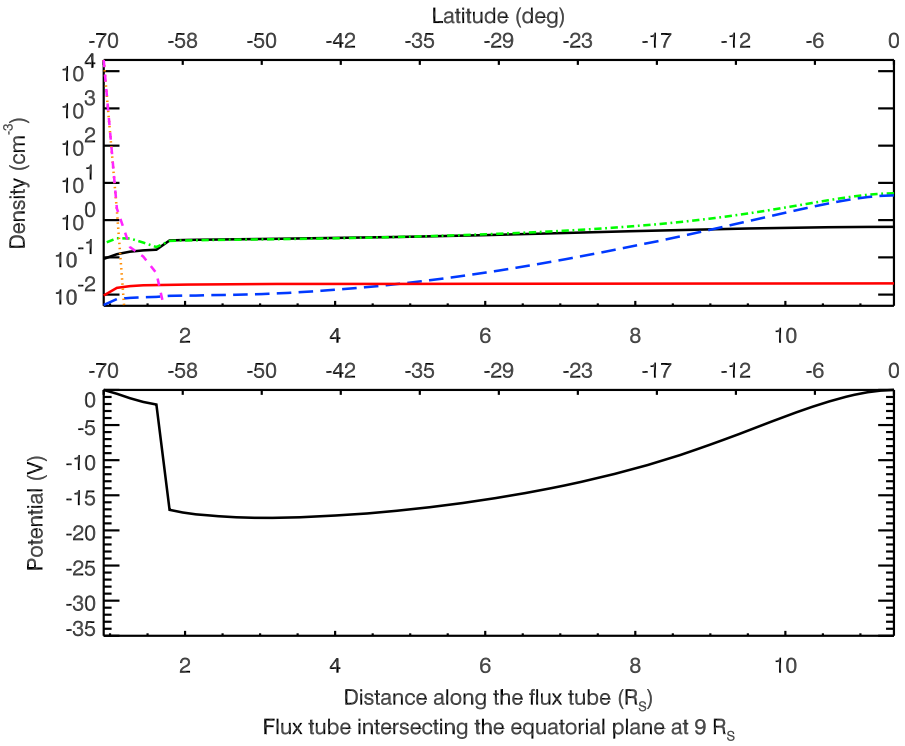

Figure 6. Same as Figure 4 but for the flux tube mapping to 9 R_S. The magnetospheric electron population boundary condition is based on the analysis of *Schippers et al.* [2012].

[34] The electron intensity profiles are shown in Figure 3c. At low precipitation energies, the cold electrons dominate the energy flux into the ionosphere, while the hot electrons deposit the majority of their flux at energies above 200 V. The respective cold and hot energy fluxes are 6.16×10^{-4} mW/m^2 and 0.323 mW/m^2 for maximum energies of 504 eV and 50 keV. When the electron intensity profiles are extrapolated past the maximum energies included in the Vlasov model to energies of 1000 keV, the net energy flux input to the ionospheric model is 0.347 mW/m^2 with a mean precipitating electron energy of 4.4 keV. At the ionosphere the field-aligned current density, $j_{||}$, is found to be 0.318 μA/m^2, with the hot electrons carrying slightly more current, $j_{||h}$ = 0.194 μA/m^2, than the cold population, $j_{||c}$ = 0.124 μA/m^2. The relative increase in the field-aligned current density carried by the hot population, compared to the $r_{eq} = 6\ R_S$ case, reflects the higher fraction of hot electrons in the magnetospheric population. At −70.0° latitude, the Pedersen conductance in the presence of electron precipitation ranges from 18.6–18.9 mho, with a reaction rate of 2 k_1^* corresponding to hard electron precipitation, consistent with the relatively large incident energy flux.

3.3.2. Case 2: Small Fraction of Hot Electrons

[35] Reanalysis of Cassini data following the recalibration of the CAPS ELS instrument [*Lewis et al.*, 2010] provides a lower fraction of hot electrons than in the original analysis. Additionally, the electron population has three components: cold, warm, and hot [*Schippers et al.*, 2012]. We use here a simplified description of the reanalyzed data which consists of two electron populations: a kappa distribution of cold electrons with a density of n_{e_c} = 5.26 cm^{-3}, temperature of T_{e_c} = 6.0 eV, and κ = 3; and a Maxwellian distribution of hot electrons with a density of n_{e_h} = 0.02 cm^{-3} and temperature of T_{e_h} = 1000.0 eV.

[36] Figure 6 shows the field-aligned density and potential structure for this 'lower-bound' case. As is clear from the density profiles, the hot electrons represent a significantly smaller percentage of the total electron density (0.3%) compared to the trended case discussed in section 3.3.1 (3%). Additionally, the temperatures of both the hot and cold magnetospheric electron populations are decreased here. The electrons have less mobility along the magnetic flux tube and thus the degree of field-aligned charge separation, and therefore the magnitude of the associated ambipolar field-aligned potential, are reduced. The maximum field-aligned potential in the lower-bound case is 18.2 V, compared to 31.4 V when a more energetic electron population is considered (Case 1, section 3.3.1).

[37] The density of the hot electrons remains nearly constant along the magnetic flux tube, while the cold electron density decreases with distance from the equatorial plane. A sharp potential drop exists at 1.8 R_S along the field line. At the ionospheric side of this drop, there exists a slight density cavity created by the acceleration of particles through the potential structure. Owing to the small fraction of hot electrons, the field-aligned current density is carried primarily by the cold electrons with $j_{||c} = 0.0795$ μA/m^2 compared with $j_{||h}$ = 0.0172 μA/m^2. The resulting total ionospheric field-aligned current density, $j_{||}$, is 0.098 μA/m^2.

[38] The hot and cold electron intensity profiles incident upon the ionosphere are shown with the trended case in Figure 3c. The mean electron precipitation energy is 1.4 keV. The cold electrons provide the majority of the energy flux at

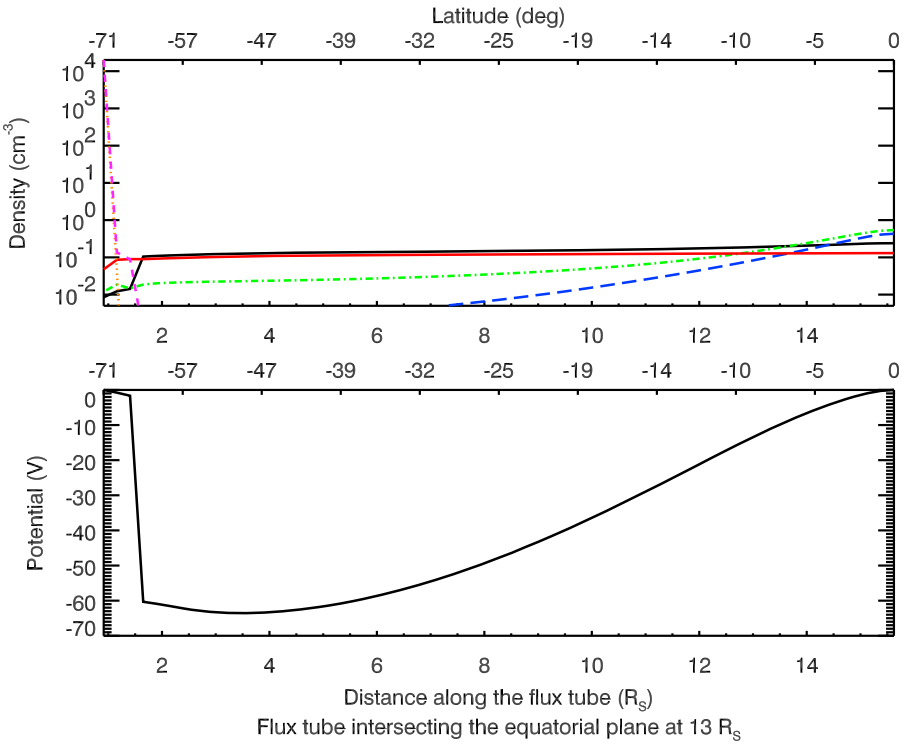

Figure 7. Same as Figure 4 but for the flux tube mapping to 13 R_S.

energies below 200 eV and are associated with an energy flux of 1.5×10^{-4} mW/m^2. At higher energies, the hot electrons dominate the precipitation with an energy flux of 0.0162 mW/m^2. Extrapolating to energies of 40 keV, the net energy flux precipitating into the ionospheric model is 0.0164 mW/m^2. The induced ionospheric Pedersen conductance at $-70°$ ranges from 4.5–5.27 mho for a prescribed effective reaction rate of 0.6 k_1^*. Comparing cases 3.3.1 and 3.3.2 emphasizes the need for reliable plasma moments for this type of analysis.

3.3.3. Case 3: *Schippers et al.* [2008]

[39] *Schippers et al.* [2008] uses Cassini CAPS/ELS and MIMI/LEMMS data for Revolution 24 of Cassini to identify an electron population that can be described as a kappa distribution of cold electrons with density of $n_{e_c} = 5.80$ cm^{-3}, temperature of $T_{e_c} = 23.6$ eV, and $\kappa = 1.86$, and a kappa distribution of hot electrons with a density of $n_{e_h} = 0.32$ cm^{-3}, approximated here as $n_{e_h} = 0.30$ cm^{-3}, temperature of $T_{e_h} = 2400.0$ eV, and $\kappa = 4.24$. We assume an ion population with a Boltzmann distribution of protons of density, $n_{H^+} = 0.7$ cm^{-3} and effective temperature of $T_{H^+} = 27.0$ eV; and a Maxwellian distribution of water group ions with a mass of $m_{W^+} = 17$ amu, density of $n_{W^+} = 5.4$ cm^{-3}, effective temperature of $T_{W^+} = 165.0$ eV, and temperature anisotropy of $T_\perp/T_\parallel = 2$ based on the analysis of *Wilson et al.* [2008].

[40] The maximum field-aligned potential is ~40 V and the structure along the magnetic flux tube is similar to that in section 3.3.1. However, owing to a combination of both the high energy (2.4 keV) and the large fraction of hot electrons (~5%), the net field-aligned current density, $j_\parallel = 0.571$ μA/m^2, is primarily carried by the hot electrons which have a field-aligned current density of $j_{\parallel h} = 0.379$ μA/m^2. Unsurprisingly, the hot electrons also dominate the net incident energy flux into the ionosphere of 0.840 mW/m^2. Using this energy flux as input into the ionospheric model, we find a Pedersen conductance of 34 mho for a prescribed effective reaction rate of 2 k_1^*, appropriate for hard auroral precipitation. This Pedersen conductance is exceptionally large, exceeding previous estimates based on Cassini observations [*Moore et al.*, 2010], which is why we do not show the full results here.

3.4. Solution for Flux Tube Intersecting 13 R_S

[41] For the flux tube mapping from $-71.6°$ latitude to $r_{eq} = 13$ R_S, the magnetospheric electron population is composed of a kappa distribution of cold electrons with a density of $n_{e_c} = 0.54$ cm^{-3}, temperature of $T_{e_c} = 19.6$ eV, and $\kappa = 1.97$; and a kappa distribution of hot electrons with a density of $n_{e_h} = 0.13$ cm^{-3}, temperature of $T_{e_h} = 1177$ eV, and $\kappa = 3.77$ [*Schippers*, 2009].

[42] The ion population is based on the analysis of *Thomsen et al.* [2010]; however we simplify their results by merging the H_2^+ population with the proton population such that the magnetospheric plasma is composed solely of protons and water group ions. The H_2^+ population has a temperature similar to the protons, 40 eV compared with 30 eV, and a significantly smaller density, 0.05 cm^{-3} relative to 0.19 cm^{-3}. As such, this simplification does not strongly affect the Vlasov solutions. The proton population is a Boltzmann distribution with a density of $n_{H^+} = 0.24$ cm^{-3} and temperature of $T_{H^+} = 30$ eV. The water group are specified as a Maxwellian distribution with a density of $n_{W^+} = 0.43$ cm^{-3}. *Thomsen et al.* [2010] calculate the effective temperature of the water group ions. For equatorial radii less than 10 R_S, where the *Thomsen et al.* [2010] and *Wilson et al.* [2008] analyses overlap, *Thomsen et al.* [2010] find that these

temperatures are consistent with the parallel temperatures of the water group ions found by *Wilson et al.* [2008]. Therefore, we set a temperature anisotropy of $T_\perp/T_\parallel = 2$ for the water group ions and, using the *Thomsen et al.* [2010] effective temperature, ~250 eV, as a parallel temperature, calculate a new 'effective' temperature of 416 eV for the water group ions.

[43] Figure 7 displays the field-aligned densities and ambipolar potential structures for the quasi-neutral solution. The hot electrons are a significant component of the magnetospheric electrons, comprising 24% of the population. Their density remains fairly constant along the flux tube while the cold electron population decays with distance off the equatorial plane. As such, the hot electrons are the dominant contributors to the ionospheric field-aligned current density with $j_{\parallel h} = 0.111$ μA/m^2 in comparison to $j_{\parallel c} = 0.0116$ μA/m^2. The total field-aligned current density at the ionosphere is $j_\parallel = 0.123$ μA/m^2.

[44] The field-aligned potential structure is similar to those presented in sections 3.1, 3.2, and 3.3. Owing to a combination of the increased centrifugal forces, and hence confinement of the heavy ions; and the increased fraction of hot electrons, and hence greater mobility of negative charged particles, the magnetospheric ambipolar potential has a maximum magnitude of 63.6 V. Nearly all of the ambipolar potential is dropped over ~0.2 R_S at a distance of 1.5 R_S along the magnetic flux tube, resulting in a narrow density cavity. This drop is more substantial than those presented in sections 3.1, 3.2, and 3.3 because of the larger magnitude of the ambipolar potential. However the location of the acceleration region remains the same, ~1.5 R_S along the magnetic flux tube, as this is where the minimum in the sum of the gravitational and centrifugal forces exists.

[45] The electron intensity profile varies from those presented earlier in that the cold electron population never dominates the incident electron flux. As expected, the minimum energy of the precipitating electrons is 63.6 V due to the sharp potential drop at 1.5 R_S. However the cold electron density is an order of magnitude less than that of the hot electrons because of the lower equatorial energy of the cold electrons in conjunction with mirror effects. The hot and cold electron energy fluxes are 0.123 mW/m^2 and 6.79×10^{-5} mW/m^2, respectively. Considering the extrapolation to energies above those considered in the numerical model, the net energy flux into the ionospheric model is 0.126 mW/m^2. The resulting Pedersen conductance at $-71.6°$ ranges from 12.7–13.2 mho for a prescribed effective reaction rate of 0.6 k_1^*.

4. Discussion

[46] The prescribed magnetic flux tubes in the model are unperturbed by the motion of satellites through the planetary magnetic field. Thus, we treat our results for the flux tube intersecting the equatorial plane at 4 R_S as appropriate to the region of the Enceladus torus downstream of the moon. At the ionospheric latitude of the magnetic field line mapping to $r_{eq} = 4$ R_S, ($-62.1°$), we calculate an energy flux incident upon the ionosphere of 0.00472 mW/m^2. An incident energy flux of 1 mW/m^2 produces 10 ± 0.2 kiloRayleighs (kR) of H_2 UV emission in a pure H_2 atmosphere [*Gerard and Singh*, 1982]. Assuming this conversion rate, our model predicts that an auroral emission of 47.2 R is excited in the absence of any field aligned acceleration apart from that owing to the ambipolar potential. This is an order of magnitude dimmer than the lowest emission Enceladus spot detected by Cassini UVIS [*Pryor et al.*, 2011]. Therefore, our model does not predict the existence of a detectable UV auroral wake emission downstream of Enceladus, consistent with the analysis of *Wannawichian et al.* [2008]. However, *Stallard et al.* [2008] detected an IR aurora at ionospheric latitudes mapping to the orbit of Enceladus that was ~25% as bright as the main auroral emission.

[47] *Grodent et al.* [2010] derived an associated energy flux of ~0.3 mW/m^2 for the midlatitude diffuse UV auroral emission mapping from 4–11 R_S. Using the double kappa description for the electron population from *Schippers et al.* [2008], we find an energy flux of ~0.8 mW/m^2 which is significantly larger than that derived from UV observations and results in an unreasonably large ionospheric Pedersen conductance of 34 mho. However, this electron distribution was determined through use of a single spacecraft revolution and the CAPS ELS instrument has since been recalibrated, resulting in a reduction of the density of the hot electron component of the magnetospheric plasma [*Lewis et al.*, 2010]. The 'trended' 9 R_S case, for which the electron parameters are derived from seven years of spacecraft data and do not account for the recalibration of the CAPS/ELS instrument, yields an electron energy flux of 0.347 mW/m^2 and is consistent with the value derived from UV observations. However, our predicted energy fluxes for the 6 R_S case, which uses the same data set as the 'trended' 9 R_S case, and 'lower-bound' 9 R_S cases fall an order of magnitude below those inferred from observations. The plasma parameters for the 'lower-bound' 9 R_S case consider the recalibration of the CAPS ELS instrument and may be more representative of the magnetospheric plasma population.

[48] Therefore, the interpretation of the driver for the midlatitude emission varies with our understanding of the magnetospheric plasma parameters. If the 'trended' densities are indeed more typical for Saturn's middle magnetosphere, then the diffuse emission is likely excited by the hot magnetospheric electron population as originally proposed by *Grodent et al.* [2010]. Yet if this is the case, the subcorotation of Saturn's magnetospheric plasma may be a mystery. As discussed in the Introduction, there are four possible limitations to the transfer of angular momentum between the planet and its magnetospheric plasma: the true ionospheric Pedersen conductance, a lack of current carriers at high magnetic latitudes which restrict the magnitude of the field-aligned currents, the rotation rate of the neutral atmosphere at the foot of the planetary magnetic field line which yields the effective Pedersen conductance, and ion-neutral friction in the magnetosphere. Initial studies based on the torque balance model presented by *Ray et al.* [2010], modified to include momentum loading from charge exchange, applied at Saturn suggest that large field-aligned current densities of 0.318 μA/m^2 should be sufficient to transfer angular momentum from Saturn to its subcorotating plasma such that the magnetospheric plasma reaches near-rigid corotation.

[49] The calculated Pedersen conductance values given in section 3 are true conductances. They do not include the relative rotation of the neutral atmosphere with respect to the planetary rotation rate. When considered in the context of

magnetosphere-ionosphere coupling, it is necessary to take into account the subcorotation of the neutral atmosphere, such that the ionospheric Pedersen conductance can be scaled accordingly [*Huang and Hill*, 1989]. At low altitudes underneath the main auroral emission, the rotation rate of neutral atmosphere relative to planetary corotation derived from the 3D STIM General Circulation Model was found to be 50% [*Galand et al.*, 2011]. This rate of neutral rotation yields an effective Pedersen conductance in the auroral region equal to half the true Pedersen conductance. At latitudes equatorward of $\sim$75°, the deviation of the neutral atmosphere from planetary corotation is expected to decrease, which would therefore result in a smaller reduction of the true Pedersen conductance. Here, we find true Pedersen conductances ranging from 18.6–18.9 mho at $-$70.0° for soft auroral precipitation. Using the scaling of 0.5 for auroral regions, this yields a lower limit for the effective Pedersen conductance of $\sim$6.3–6.8 mho. Such large Pedersen conductances are not expected to significantly limit the field-aligned currents running from Saturn to its magnetosphere.

[50] Neither the large field-aligned current density, nor the Pedersen conductance, significantly limit the transfer of angular momentum and are hence inconsistent with the 20% subcorotation of the magnetospheric plasma from $\sim$4–10 R_S found by Cassini [*Wilson et al.*, 2008; *Thomsen et al.*, 2010] unless: (1) the corresponding planetary ionosphere from $-$62° to $-$70° also subcorotates by 20% or (2) significant field-aligned potentials exist, which allow for differential rotation between the ionosphere and magnetosphere. For latitudes spanning $\sim-$62° to $-$70°, a 20% lag from corotation in the coupling region corresponds to westward velocities of $\sim$1000 m/s to $\sim$700 m/s. Line of sight ionospheric angular velocities derived from H_3^+ observations indicate westward flows of 1000–2000 m/s between $-$73° and $-$65° [*Stallard et al.*, 2007]. Therefore, the deviation in corotation of the magnetospheric plasma is consistent with the observed deviation from corotation of the ionosphere. It should be noted that the neutral atmosphere will not have the same angular velocity as the ionosphere since the neutral atmosphere and ionosphere are coupled through ion-neutral collisions and therefore can 'slip' relative to one another.

[51] On the other hand, if 'lower-bound' magnetospheric populations are more typical, then field-aligned acceleration may be required to provide the necessary energy flux to generate this midlatitude auroral emission. Additionally, the reduced field-aligned current density associated with the 'lower-bound' magnetospheric densities may not be enough to transfer angular momentum from Saturn to its magnetospheric plasma. As such, field-aligned potentials may develop at high-latitudes to provide the necessary angular momentum to the magnetospheric plasma [*Ray et al.*, 2010]. Currently, due to the lack of any significant hydrocarbon absorption of auroral emissions observed at midlatitudes, it is not possible to accurately determine the energy of the precipitating electrons that create the sub-auroral UV emission. However, despite this lack of hydrocarbon absorption, an upper bound for the precipitating electron energy may still be determined. In the midlatitude regions studied here, precipitating electrons require a mean energy of $\sim$2 keV to reach the hydrocarbon layer. A net field-aligned potential drop of 1.5 kV produces an incident electron energy flux of $\sim$0.25 mW/m^2 (L. C. Ray, manuscript in preparation, 2012). This is within the energy range where UV emission would be generated above the hydrocarbon layer. If this is the case, then the sub-auroral diffuse emission may be the signature of corotation breakdown in Saturn's magnetosphere, similar to Jupiter's main auroral emission [*Ray et al.*, 2010]. This remains a topic for further study.

[52] The 6 R_S and 13 R_S cases yield similar ionospheric field-aligned current densities; however their energy fluxes differ by an order of magnitude. This is due to the larger fraction of hot electrons at 13 R_S which produces a dominant contribution to the energy flux compared to that of the cold electrons. Ambipolar potentials of 8.1 V and 63.6 V restrict the motion of the cold electron populations, which have temperatures of 2.0 eV and 19.6 eV at 6 R_S and 13 R_S, respectively.

[53] *Sittler et al.* [2008] calculated field-aligned density profiles for electrons, protons and water group ions at L shells of 4, 6.3 and 10 by applying ion-electron force balance in a dipole magnetic field. Our field-aligned density profiles are consistent with the *Sittler et al.* [2008] results, although we calculate a peak magnitude of the proton density that is reduced by a factor of two, compared to their prediction. One possible reason for this discrepancy is that our model prescribes a non-dipolar magnetic structure which increases the mirror ratio from the equatorial plane to the planet, hence restricting the mobility of the plasma in the field-aligned direction. Another cause may be the specification of a 0 V net potential drop between the ionosphere and magnetosphere. A result of this requirement is that the magnetospheric ambipolar potential must be 'dropped' along the flux tube, with the narrow width of the drop a consequence of the gravitational and centrifugal profiles. The narrow potential drop produces a density cavity.

[54] In the physical system, there may exist a net potential drop between the ionosphere and magnetosphere. We assume a 0 V net potential drop in this analysis to easily compare the different flux tubes and to represent perfect magnetosphere-ionosphere coupling throughout the middle magnetosphere. For the two regions to be perfectly coupled, the perpendicular gradient (latitudinal or radial gradient depending on an ionospheric or magnetospheric perspective) of the field-aligned potential must be zero [*Ergun et al.*, 2009; *Ray et al.*, 2010]. In the case that the field-aligned potential is smoothly varying, the magnitude of the net field-aligned potential drop is approximately given by difference in the magnetospheric and ionospheric ambipolar potentials, resulting in a perpendicular gradient in the parallel potential. However, this gradient is on the order of a few volts per R_S and therefore unlikely to strongly decouple the system. If a smoothly varying field-aligned potential profile, resulting in a net potential drop between the ionosphere and magnetosphere, exists, then the precipitating electron energy flux calculated in this analysis - which is dominated by the hot electron population - is qualitatively unaffected, decreasing by $\sim$5%. The field-aligned current density at the ionosphere, which is predominately carried by the cold electrons, can be reduced by as much as a factor of two as the cold electrons are no longer accelerated at high latitudes.

[55] The variation in the ambipolar potential between the 'trended' and 'lower-bound' cases for the flux tube

Table 3. Ionospheric Parameters for All Runs[a]

R_S	Θ	$j_{\|\|i}$ (μA/m^2)	Energy Flux (mW/m^2)	Pedersen Conductance (mho)	k_Γ^* Scaling
4	−62.1°	1.514	0.00472	3.0–3.8	0.6
6	−67.2°	0.186	0.0248	5.06–5.85	0.6
9[b]	−70.0°	0.318	0.347	18.6–18.9	2
9[c]	−70.0°	0.098	0.0164	4.4–5.2	0.25
13	−71.6°	0.123	0.126	12.7–13.2	0.6

[a]The Pedersen conductance range shown is for midnight - noon local time.
[b]Trended densities.
[c]Lower limit.

intersecting 9 R_S reflects changes in the magnetospheric electron population. In addition to smaller densities in the 'lower-bound' case, the electron temperatures are also lower. As such, the charge separation that develops along the magnetic flux tube is reduced and hence a lower ambipolar potential is required to maintain charge-neutrality.

[56] It should be noted that the solutions to the Vlasov model are non-unique. The location of the field-aligned potential drop can shift slightly in location, as much as one spatial cell. However, our results remain qualitatively sound and the maximum magnitudes of the ambipolar potential and field-aligned current density are not significantly affected by this shift. The sensitivity to the initial plasma parameters plays a much larger role in the variation between solutions, as displayed in sections 3.3.1, 3.3.2, and 3.3.3.

5. Conclusions

[57] The field-aligned currents that couple Saturn's magnetosphere and ionosphere vary strongly with radial distance as summarized in Table 3. This is expected as both the centrifugal forces and mirror ratios between the magnetospheric equatorial plane and planetary ionosphere increase with radial distance. Additionally, there exist strong variations in the magnetospheric plasma population, which when considered alone, affect the ionospheric results. We draw the following conclusions:

[58] 1. The magnitude of the field-aligned currents and electron energy flux depends on the magnetospheric plasma population.

[59] 2. Ambipolar potentials on the order of ∼10 to ∼40 V develop, nearly all of which are dropped over a narrow width (∼0.5 R_S) at high magnetic latitudes.

[60] 3. In the middle magnetosphere, Saturn's magnetosphere-ionosphere coupling system is not expected to be limited by the ionospheric Pedersen conductance which ranges from 3–18.9 mho.

[61] 4. The ionospheric electron energy flux at −70° latitude using 'trended' magnetospheric parameters, 0.347 mW/m^2, is consistent with that derived from observations [*Grodent et al.*, 2010] however the magnetospheric inputs [*Schippers et al.*, 2008] were derived before the recalibration of the CAPS/ELS instrument [*Lewis et al.*, 2010].

[62] 5. The ionospheric electron energy flux for the case with a 'lower-bound' magnetospheric population is an order of magnitude less than that derived by auroral UV observations indicating that the observed emission may require that the electron population is accelerated at high latitudes.

[63] Understanding the composition and, in particular, the density of the magnetospheric plasma population is key in describing magnetosphere-ionosphere coupling in the Saturnian system. Precipitation from the magnetospheric plasma enhances the ionospheric Pedersen conductance, allowing for enhanced coupling between the two regions. This phenomenon could also explain the UV auroral emissions equatorward of the main auroral emission; however this depends on the equatorial magnetospheric plasma densities derived from the Cassini spacecraft.

[64] **Acknowledgments.** L.C.R. and M.G. are supported by the Science and Technology Facilities Council (STFC) rolling grant to Imperial College London. L.C.R. received travel support from the RAS and, along with M.G., from the EU/DEPTH grant to discuss with colleagues. L.M. is supported by a NASA CDAP grant. B.F. is supported by through the NASA NESSF program. We thank Ingo Mueller-Wodarg very much for very helpful discussions and for supplying us the neutral atmospheric density profiles. We are also indebted to Patricia Schippers for supplying the electron properties in the middle magnetosphere. Finally, we thank the reviewers for their comments.

[65] Masaki Fujimoto thanks the reviewers for their assistance in evaluating this paper.

References

Achilleos, N., C. S. Arridge, C. Bertucci, C. M. Jackman, M. K. Dougherty, K. K. Khurana, and C. T. Russell (2008), Large-scale dynamics of Saturn's magnetopause: Observations by Cassini, *J. Geophys. Res.*, *113*, A11209, doi:10.1029/2008JA013265.

Badman, S. V., S. W. H. Cowley, J.-C. Gérard, and D. Grodent (2006), A statistical analysis of the location and width of Saturn's southern auroras, *Ann. Geophys.*, *24*, 3533–3545.

Badman, S. V., C. Tao, A. Grocott, S. Kasahara, H. Melin, R. H. Brown, K. H. Baines, M. Fujimoto, and T. Stallard (2011), Cassini VIMS observations of latitudinal and hemispheric variations in Saturn's infrared auroral intensity, *Icarus*, *216*, 367–375.

Bagenal, F., and P. A. Delamere (2011), Flow of mass and energy in the magnetospheres of Jupiter and Saturn, *J. Geophys. Res.*, *116*, A05209, doi:10.1029/2010JA016294.

Baumjohann, W., and R. A. Treumann (1996), *Basic Space Plasma Physics*, Imperial College Press, London.

Brown, R. A. (1983), Observed departure of the Io plasma torus from rigid corotation with Jupiter, *Astrophys. J.*, *268*, L47–L50.

Bunce, E. J., S. W. H. Cowley, I. I. Alexeev, C. S. Arridge, M. K. Dougherty, J. D. Nichols, and C. T. Russell (2007), Cassini observations of the variation of Saturn's ring current parameters with system size, *J. Geophys. Res.*, *112*, A10202, doi:10.1029/2007JA012275.

Bunce, E. J., C. S. Arridge, S. W. H. Cowley, and M. K. Dougherty (2008), Magnetic field structure of Saturn's dayside magnetosphere and its mapping to the ionosphere: Results from ring current modeling, *J. Geophys. Res.*, *113*, A02207, doi:10.1029/2007JA012538.

Clarke, J. T., D. Grodent, S. W. H. Cowley, E. J. Bunce, P. Zarka, J. E. P. Connerney, and T. Satoh (2004), Jupiter's aurora, in *Jupiter. The Planet, Satellites and Magnetosphere*, pp. 639–670, Cambridge Univ. Press, Cambridge, U. K.

Clarke, J. T., et al. (2009), Response of Jupiter's and Saturn's auroral activity to the solar wind, *J. Geophys. Res.*, *114*, A05210, doi:10.1029/2008JA013694.

Cowley, S. W. H., and E. J. Bunce (2001), Origin of the main auroral oval in Jupiter's coupled magnetosphere-ionosphere system, *Planet. Space Sci.*, *49*, 1067–1088.

Cowley, S. W. H., and E. J. Bunce (2003), Corotation-driven magnetosphere-ionosphere coupling currents in Saturn's magnetosphere and their relation to the auroras, *Ann. Geophys.*, *21*, 1691–1707.

Cowley, S., E. Bunce, and R. Prangé (2004), Saturn's polar ionospheric flows and their relation to the main auroral oval, *Ann. Geophys.*, *22*, 1379–1394.

Cowley, S. W. H., C. S. Arridge, E. J. Bunce, J. T. Clarke, A. J. Coates, M. K. Dougherty, J.-C. Gérard, D. Grodent, J. D. Nichols, and D. L. Talboys (2008), Auroral current systems in Saturn's magnetosphere: Comparison of theoretical models with Cassini and HST observations, *Ann. Geophys.*, *26*, 2613–2630.

Delamere, P. A., F. Bagenal, R. Ergun, and Y.-J. Su (2003), Momentum transfer between the Io plasma wake and Jupiter's ionosphere, *J. Geophys. Res.*, *108*(A6), 1241, doi:10.1029/2002JA009530.

Delamere, P. A., F. Bagenal, V. Dols, and L. C. Ray (2007), Saturn's neutral torus versus Jupiter's plasma torus, *Geophys. Res. Lett.*, *34*, L09105, doi:10.1029/2007GL029437.

Dougherty, M. K., et al. (2005), Cassini magnetometer observations during Saturn orbit insertion, *Science*, *307*, 1266–1270.

Ergun, R. E., C. W. Carlson, J. P. McFadden, F. S. Mozer, and R. J. Strangeway (2000), Parallel electric fields in discrete arcs, *Geophys. Res. Lett.*, *27*, 4053–4056.

Ergun, R. E., L. Ray, P. A. Delamere, F. Bagenal, V. Dols, and Y.-J. Su (2009), Generation of parallel electric fields in the Jupiter–Io torus wake region, *J. Geophys. Res.*, *114*, A05201, doi:10.1029/2008JA013968.

Fleshman, B. L., P. A. Delamere, and F. Bagenal (2010), A sensitivity study of the Enceladus torus, *J. Geophys. Res.*, *115*, E04007, doi:10.1029/2009JE003372.

Galand, M., L. Moore, B. Charnay, I. Mueller-Wodarg, and M. Mendillo (2009), Solar primary and secondary ionization at Saturn, *J. Geophys. Res.*, *114*, A06313, doi:10.1029/2008JA013981.

Galand, M., L. Moore, I. Mueller-Wodarg, M. Mendillo, and S. Miller (2011), Response of Saturn's auroral ionosphere to electron precipitation: Electron density, electron temperature, and electrical conductivity, *J. Geophys. Res.*, *116*, A09306, doi:10.1029/2010JA016412.

Gerard, J.-C., and V. Singh (1982), A model of energy deposition of energetic electrons and EUV emission in the Jovian and Saturnian atmospheres and implications, *J. Geophys. Res.*, *87*, 4525–4532.

Grodent, D., A. Radioti, B. Bonfond, and J.-C. Gérard (2010), On the origin of Saturn's outer auroral emission, *J. Geophys. Res.*, *115*, A08219, doi:10.1029/2009JA014901.

Hansen, C. J., et al. (2011), The composition and structure of the Enceladus plume, *Geophys. Res. Lett.*, *38*, L11202, doi:10.1029/2011GL047415.

Hill, T. W. (1979), Inertial limit on corotation, *J. Geophys. Res.*, *84*, 6554–6558.

Hill, T. W. (2001), The Jovian auroral oval, *J. Geophys. Res.*, *106*, 8101–8108.

Hill, T. W., and F. C. Michel (1976), Heavy ions from the Galilean satellites and the centrifugal distortion of the Jovian magnetosphere, *J. Geophys. Res.*, *81*, 4561–4565.

Hill, T. W., and V. M. Vasyliūnas (2002), Jovian auroral signature of Io's corotational wake, *J. Geophys. Res.*, *107*(A12), 1464, doi:10.1029/2002JA009514.

Huang, T. S., and T. W. Hill (1989), Corotation lag of the Jovian atmosphere, ionosphere, and magnetosphere, *J. Geophys. Res.*, *94*, 3761–3765.

Huestis, D. L. (2008), Hydrogen collisions in planetary atmospheres, ionospheres, and magnetospheres, *Planet. Space Sci.*, *56*, 1733–1743.

Kliore, A. J., A. F. Nagy, E. A. Marouf, A. Anabtawi, E. Barbinis, D. U. Fleischman, and D. S. Kahan (2009), Midlatitude and high-latitude electron density profiles in the ionosphere of Saturn obtained by Cassini radio occultation observations, *J. Geophys. Res.*, *114*, A04315, doi:10.1029/2008JA013900.

Kurth, W. S., et al. (2009), Auroral processes, in *Saturn From Cassini-Huygens*, pp. 333–374, Springer, Dordrecht, Netherlands.

Lewis, G. R., et al. (2010), The calibration of the Cassini-Huygens CAPS Electron Spectrometer, *Planet. Space Sci.*, *58*, 427–436.

Melin, H., T. Stallard, S. Miller, J. Gustin, M. Galand, S. V. Badman, W. R. Pryor, J. O'Donoghue, R. H. Brown, and K. H. Baines (2011), Simultaneous Cassini VIMS and UVIS observations of Saturn's southern aurora: Comparing emissions from H, H_2 and H_3^+ at a high spatial resolution, *Geophys. Res. Lett.*, *38*, L15203, doi:10.1029/2011GL048457.

Moore, L. E., M. Mendillo, I. C. F. Müller-Wodarg, and D. L. Murr (2004), Modeling of global variations and ring shadowing in Saturn's ionosphere, *Icarus*, *172*, 503–520.

Moore, L., M. Galand, I. Mueller-Wodarg, R. Yelle, and M. Mendillo (2008), Plasma temperatures in Saturn's ionosphere, *J. Geophys. Res.*, *113*, A10306, doi:10.1029/2008JA013373.

Moore, L., I. Mueller-Wodarg, M. Galand, A. Kliore, and M. Mendillo (2010), Latitudinal variations in Saturn's ionosphere: Cassini measurements and model comparisons, *J. Geophys. Res.*, *115*, A11317, doi:10.1029/2010JA015692.

Moses, J. I., and S. F. Bass (2000), The effects of external material on the chemistry and structure of Saturn's ionosphere, *J. Geophys. Res.*, *105*, 7013–7052.

Mueller-Wodarg, I. M. (2012), STIM GCM, *Icarus*, *25*, 1629–1632.

Nichols, J., and S. Cowley (2004), Magnetosphere-ionosphere coupling currents in Jupiter's middle magnetosphere: Effect of precipitation-induced enhancement of the ionospheric Pedersen conductivity, *Ann. Geophys.*, *22*, 1799–1827.

Nichols, J. D., and S. W. H. Cowley (2005), Magnetosphere-ionosphere coupling currents in Jupiter's middle magnetosphere: Effect of magnetosphere-ionosphere decoupling by field-aligned auroral voltages, *Ann. Geophys.*, *23*, 799–808.

Persoon, A. M., et al. (2009), A diffusive equilibrium model for the plasma density in Saturn's magnetosphere, *J. Geophys. Res.*, *114*, A04211, doi:10.1029/2008JA013912.

Pontius, D. H., Jr., and T. W. Hill (1982), Departure from corotation of the Io plasma torus: Local plasma production, *Geophys. Res. Lett.*, *9*, 1321–1324.

Pontius, D. H., Jr., and T. W. Hill (2006), Enceladus: A significant plasma source for Saturn's magnetosphere, *J. Geophys. Res.*, *111*, A09214, doi:10.1029/2006JA011674.

Pontius, D. H., Jr., and T. W. Hill (2009), Plasma mass loading from the extended neutral gas torus of Enceladus as inferred from the observed plasma corotation lag, *Geophys. Res. Lett.*, *36*, L23103, doi:10.1029/2009GL041030.

Pryor, W. R., et al. (2011), The auroral footprint of Enceladus on Saturn, *Nature*, *472*, 331–333.

Ray, L. C., Y.-J. Su, R. E. Ergun, P. A. Delamere, and F. Bagenal (2009), Current-voltage relation of a centrifugally confined plasma, *J. Geophys. Res.*, *114*, A04214, doi:10.1029/2008JA013969.

Ray, L. C., R. E. Ergun, P. A. Delamere, and F. Bagenal (2010), Magnetosphere-ionosphere coupling at Jupiter: Effect of field-aligned potentials on angular momentum transport, *J. Geophys. Res.*, *115*, A09211, doi:10.1029/2010JA015423.

Richardson, J. D. (1998), Thermal plasma and neutral gas in Saturn's magnetosphere, *Rev. Geophys.*, *36*, 501–524.

Richardson, J. D., and S. Jurac (2004), A self-consistent model of plasma and neutrals at Saturn: The ion tori, *Geophys. Res. Lett.*, *31*, L24803, doi:10.1029/2004GL020959.

Saur, J., B. H. Mauk, A. Kaßner, and F. M. Neubauer (2004), A model for the azimuthal plasma velocity in Saturn's magnetosphere, *J. Geophys. Res.*, *109*, A05217, doi:10.1029/2003JA010207.

Schippers, P. (2009), Etude de l'équilibre et de la circulation des populations d'électrons dans la magnétosphère de Saturne à l'aide des données multi-instrumentales de la sonde Cassin-Huygens, PhD thesis, Univ. de Toulouse, Toulouse, France.

Schippers, P., et al. (2008), Multi-instrument analysis of electron populations in Saturn's magnetosphere, *J. Geophys. Res.*, *113*, A07208, doi:10.1029/2008JA013098.

Schippers, P., N. André, D. A. Gurnett, G. R. Lewis, A. M. Persoon, and A. J. Coates (2012), Identification of electron field-aligned current systems in Saturn's magnetosphere, *J. Geophys. Res.*, *117*, A05204, doi:10.1029/2011JA017352.

Sittler, E. C., Jr., M. F. Blanc, and J. D. Richardson (2006), Proposed model for Saturn's auroral response to the solar wind: Centrifugal instability model, *J. Geophys. Res.*, *111*, A06208, doi:10.1029/2005JA011191.

Sittler, E. C., et al. (2008), Ion and neutral sources and sinks within Saturn's inner magnetosphere: Cassini results, *Planet. Space Sci.*, *56*, 3–18.

Stallard, T., C. Smith, S. Miller, H. Melin, M. Lystrup, A. Aylward, N. Achilleos, and M. Dougherty (2007), Saturn's auroral/polar H_3^+ infrared emission. II. A comparison with plasma flow models, *Icarus*, *191*, 678–690.

Stallard, T., S. Miller, H. Melin, M. Lystrup, S. W. H. Cowley, E. J. Bunce, N. Achilleos, and M. Dougherty (2008), Jovian-like aurorae on Saturn, *Nature*, *453*, 1083–1085.

Stallard, T., H. Melin, S. W. H. Cowley, S. Miller, and M. B. Lystrup (2010), Location and magnetospheric mapping of Saturn's mid-latitude infrared auroral oval, *Astrophys. J. Lett.*, *722*, L85–L89.

Su, Y.-J., R. E. Ergun, F. Bagenal, and P. A. Delamere (2003), Io-related Jovian auroral arcs: Modeling parallel electric fields, *J. Geophys. Res.*, *108*(A2), 1094, doi:10.1029/2002JA009247.

Thomsen, M. F., D. B. Reisenfeld, D. M. Delapp, R. L. Tokar, D. T. Young, F. J. Crary, E. C. Sittler, M. A. McGraw, and J. D. Williams (2010), Survey of ion plasma parameters in Saturn's magnetosphere, *J. Geophys. Res.*, *115*, A10220, doi:10.1029/2010JA015267.

Wannawichian, S., J. T. Clarke, and D. H. Pontius Jr. (2008), Interaction evidence between Enceladus' atmosphere and Saturn's magnetosphere, *J. Geophys. Res.*, *113*, A07217, doi:10.1029/2007JA012899.

Wilson, R. J., R. L. Tokar, M. G. Henderson, T. W. Hill, M. F. Thomsen, and D. H. Pontius Jr. (2008), Cassini plasma spectrometer thermal ion measurements in Saturn's inner magnetosphere, *J. Geophys. Res.*, *113*, A12218, doi:10.1029/2008JA013486.

Wilson, R. J., R. L. Tokar, and M. G. Henderson (2009), Thermal ion flow in Saturn's inner magnetosphere measured by the Cassini plasma spectrometer: A signature of the Enceladus torus?, *Geophys. Res. Lett.*, *36*, L23104, doi:10.1029/2009GL040225.